REPORT DOCUMENTATION PAGE

Form Approved OMB NO. 0704-0188

1. REPORT DATE (DD-MM-YYYY)	2. REPORT TYPE	3. DATES COVERED (From - To)
	New Reprint	-

4. TITLE AND SUBTITLE
Computational Modeling of Microstructural-Evolution in AISI 1005 Steel During Gas Metal Arc Butt Welding

5a. CONTRACT NUMBER
W911NF-11-1-0207

5b. GRANT NUMBER

5c. PROGRAM ELEMENT NUMBER
622105

6. AUTHORS
M. Grujicic, S. Ramaswami, J. S. Snipes, R. Yavari, A. Arakere, C.-F. Yen, B. A. Cheeseman

5d. PROJECT NUMBER

5e. TASK NUMBER

5f. WORK UNIT NUMBER

7. PERFORMING ORGANIZATION NAMES AND ADDRESSES
Clemson University
Office of Sponsored Programs
300 Brackett Hall, Box 345702
Clemson, SC 29634 -5702

8. PERFORMING ORGANIZATION REPORT NUMBER

9. SPONSORING/MONITORING AGENCY NAME(S) AND ADDRESS(ES)
U.S. Army Research Office
P.O. Box 12211
Research Triangle Park, NC 27709-2211

10. SPONSOR/MONITOR'S ACRONYM(S)
ARO

11. SPONSOR/MONITOR'S REPORT NUMBER(S)
57228-EG.12

12. DISTRIBUTION AVAILIBILITY STATEMENT
Approved for public release; distribution is unlimited.

13. SUPPLEMENTARY NOTES
The views, opinions and/or findings contained in this report are those of the author(s) and should not contrued as an official Department of the Army position, policy or decision, unless so designated by other documentation.

14. ABSTRACT
A fully coupled (two-way), transient, thermal-mechanical finite-element procedure is developed to model conventional gas metal arc welding (GMAW) butt-joining process. Two-way thermal-mechanical coupling is achieved by making the mechanical material model of the workpiece and the weld temperaturedependent and by allowing the potential work of plastic deformation resulting from large thermal gradients to be dissipated in the form of heat. To account for the heat losses from the weld into the surroundings, heat transfer effects associated

15. SUBJECT TERMS
AISI 1005, finite-element analysis, gas metal arcwelding (GMAW), microstructural-evolution

16. SECURITY CLASSIFICATION OF:			17. LIMITATION OF ABSTRACT	15. NUMBER OF PAGES	19a. NAME OF RESPONSIBLE PERSON
a. REPORT	b. ABSTRACT	c. THIS PAGE			Mica Grujicic
UU	UU	UU	UU		19b. TELEPHONE NUMBER 864-656-5639

Report Title

Computational Modeling of Microstructural-Evolution in AISI 1005 Steel During Gas Metal Arc Butt Welding

ABSTRACT

A fully coupled (two-way), transient, thermal-mechanical finite-element procedure is developed to model conventional gas metal arc welding (GMAW) butt-joining process. Two-way thermal-mechanical coupling is achieved by making the mechanical material model of the workpiece and the weld temperaturedependent and by allowing the potential work of plastic deformation resulting from large thermal gradients to be dissipated in the form of heat. To account for the heat losses from the weld into the surroundings, heat transfer effects associated with natural convection and radiation to the environment and thermal-heat conduction to the adjacent workpiece material are considered. The procedure is next combined with the basic physical-metallurgy concepts and principles and applied to a prototypical (plain) low-carbon steel (AISI 1005) to predict the distribution of various crystalline phases within the as-welded material microstructure in different fusion zone and heat-affected zone locations, under given GMAW-process parameters. The results obtained are compared with available open-literature experimental data to provide validation/verification for the proposed GMAW modeling effort.

REPORT DOCUMENTATION PAGE (SF298)
(Continuation Sheet)

Continuation for Block 13

ARO Report Number 57228.12-EG
Computational Modeling of Microstructural-Evolu ...

Block 13: Supplementary Note

Approved for public release; distribution is unlimited.

JMEPEG (2013) 22:1209–1222
DOI: 10.1007/s11665-012-0402-1

1059-9495/$19.00

Computational Modeling of Microstructural-Evolution in AISI 1005 Steel During Gas Metal Arc Butt Welding

M. Grujicic, S. Ramaswami, J.S. Snipes, R. Yavari, A. Arakere, C.-F. Yen, and B.A. Cheeseman

(Submitted July 13, 2012; published online October 2, 2012)

A fully coupled (two-way), transient, thermal-mechanical finite-element procedure is developed to model conventional gas metal arc welding (GMAW) butt-joining process. Two-way thermal-mechanical coupling is achieved by making the mechanical material model of the workpiece and the weld temperature-dependent and by allowing the potential work of plastic deformation resulting from large thermal gradients to be dissipated in the form of heat. To account for the heat losses from the weld into the surroundings, heat transfer effects associated with natural convection and radiation to the environment and thermal-heat conduction to the adjacent workpiece material are considered. The procedure is next combined with the basic physical-metallurgy concepts and principles and applied to a prototypical (plain) low-carbon steel (AISI 1005) to predict the distribution of various crystalline phases within the as-welded material microstructure in different fusion zone and heat-affected zone locations, under given GMAW-process parameters. The results obtained are compared with available open-literature experimental data to provide validation/verification for the proposed GMAW modeling effort.

Keywords AISI 1005, finite-element analysis, gas metal arc welding (GMAW), microstructural-evolution

1. Introduction

In this study, advanced coupled thermal-mechanical finite-element methods and tools are combined with basic physical-metallurgy concepts and principles to investigate microstructural-evolution in a prototypical steel-weldment structure welded using a conventional gas metal arc welding (GMAW) process. It is believed that this approach may help design welds and identify ''optimum'' welding-process parameters which could yield weldments with superior mechanical properties. Thus, the main aspects of this study include: (a) the basics of the GMAW process; (b) essential features of the microstructural evolution in steel weldments; and (c) an overview of the main past efforts dealing with modeling of the fusion-based welding processes and the associated microstructural-evolution. A brief overview of these aspects is presented in the remainder of this section.

1.1 The Basics of GMAW

GMAW is one of the fusion-welding processes in which: (a) the required heat is produced by an electrical arc established between a continuously fed filler-metal wire-shape consumable electrode and the workpiece components to be joined; and (b) weld protection from the environment during the welding process is attained exclusively via the use of an externally supplied (shielding) gas/mixture of gases (Ref 1). A schematic of the basic gas metal arc butt-welding process with all its major components labeled is shown in Fig. 1. The process is normally automated with respect to the attainment of a stable electrical arc (through the control of the automated feeding of the filler-metal wire) and, when the remaining aspects of the process are not automated, the welder is required to provide/control only the input regarding welding-gun positioning, guidance, and travel speed.

The main advantages of the GMAW process can be summarized as: (a) it can be used for welding most of the commercially available metallic materials, in particular, steels (including stainless steels), super alloys, aluminum alloys, etc.; (b) welding can be carried out in any standard position such as horizontal, inclined, vertical, and overhead; (c) the process produces clean welds due to the use of the externally supplied shielding gas; (d) it enables relatively high welding speeds, in particular, in the case of thicker weld sections; (e) high level of process robustness due to the short and stable character of the arc; (f) relatively high (93-98%) electrode-utilization efficiency; and (g) it is highly amenable to process automation. The main limitations/shortcomings of the GMAW process can be summarized as: (a) it may not be suitable for joining highly reactive/oxidation-prone metallic materials; (b) due to the substantial heat input and the attainment of high temperatures, it may cause significant changes in the microstructure/properties of the welded components in the regions adjacent to the weld (the so-called heat-affected zone, HAZ); (c) the weld region (also known as fusion zone, FZ) may possess inferior material properties relative to the ones found in the remainder of the weldment; and (d) it may not be suited for producing complex and small welds due to the bulky nature of the GMAW gun.

During the GMAW process, the filler metal is transferred from the feed wire into the gap between adjoining components.

M. Grujicic, S. Ramaswami, J.S. Snipes, R. Yavari, and **A. Arakere**, Department of Mechanical Engineering, Clemson University, 241 Engineering Innovation Building, Clemson, SC 29634-0921; and **C.-F. Yen** and **B.A. Cheeseman**, Army Research Laboratory— Survivability Materials Branch, Proving Ground, Aberdeen, MD 21005-5069. Contact e-mail: gmica@clemson.edu.

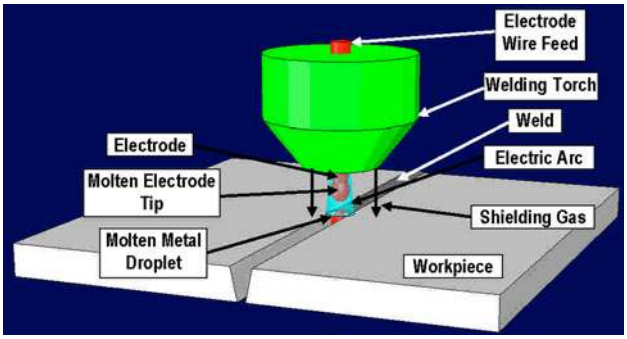

Fig. 1 A schematic representation of the conventional GMAW process

Depending on the welding-process conditions, one can distinguish between five basic modes of metal transfer (Ref 1): (a) *short-circuiting* in this case, metal is transferred during repeated (50-250 times per second) short circuits (defined as periods within which the electrode is in direct contact with the weld pool and, hence, the arc is absent). The condition required to achieve this mode of transfer is that the feed rate exceeds the electrode melt rate. The overall heat input is relatively low in this case so that this mode of metal transfer produces a shallow, fast-freezing weld puddle. Consequently (i) this process may not be suitable for welding thick workpieces; (ii) it enables welding in all positions; (iii) it can be used in sheet-metal welding applications; and (iv) it minimizes the tendency for weldment distortions and burn-throughs; (b) *globular* in this case, molten-metal is transferred in the form of large drops (typical size is 2-4 times the electrode diameter) and, to achieve this transfer mode, the arc voltage/current should be placed between the short-circuiting and spray transfer/mode counterparts. Typically, using carbon dioxide as a shielding gas promotes this mode of metal transfer; (c) *spray* in this case, as a result of the increase in the welding current, the average size of the molten-metal droplets being transferred, decreases, while the number-based transfer rate increases to a value that causes formation of an axially directed molten-metal spray; (d) *pulsed* in this case, welding voltage is cycled at a high frequency (several hundred times per second) about a mean value (sufficiently high to produce a steady arc but not high enough to produce metal transfer) and metal transfer is accomplished only at peak levels of the welding voltage. The process (i) enables a more direct control of the position rate, through the selection of the peak voltage and frequency; (ii) is characterized by an overall lower heat input; and (iii) enables welding to be carried out in all positions; and (e) *high current density* in this case, a unique combination of high wire/electrode feed rate, electrode length (a longer length causes higher temperature and, in turn, filler-wire tip melting), and shielding gas (a proper selection of the shielding gas can increase molten-metal surface tension, promoting droplet formation at the molten electrode-tip) is used to obtain a particular state of the arc which enables significantly higher molten-metal-transfer rates. At lower welding currents and in the presence of helium-/carbon dioxide-rich shielding gases, non-rotational version of this metal-transfer mode is observed which is characterized by: (i) narrower/stationary, axial arc; and (ii) localized, deeper FZ. On the other hand, at higher welding currents, rotational version of this metal-transfer mode is observed, which is characterized by: (i) wider, helically moving rotational arc; and (ii) wider and shallower FZ.

The main GMAW-process parameters can be identified as (Ref 1): (a) welding current/voltage temporal profile and magnitude; (b) filler-wire material and geometrical dimensions; (c) electrode length; (d) feed rate; (e) electrode travel speed; (f) shielding gas type/composition; (g) welding-components material(s); and (h) weld type/geometry and size.

1.2 Steel-Weldment Microstructural-Evolution During the Welding Process

As discussed above, during GMAW, the filler metal is melted and transferred into the gap separating the components being welded. The molten-metal within the resulting weld pool is subjected to electro-magnetic stirring/mixing, a process which greatly affects heat transfer within the weld pool and, in turn, spatial distribution of the temperature and thermal history of the material in the weld region (Ref 2). As the electrode advances along the weld line, the previously formed weld pool begins to cool and ultimately solidifies. Following complete solidification of the material within the weld pool, solid material within the resulting FZ typically undergoes a number of (material-system and thermal-history dependent) solid-state phase transformations and microstructural-evolution/rearrangement processes (Ref 3-5). Simultaneously, the material in the HAZ experiences an exposure to high temperatures and subsequent cooling, and this thermal history also gives rise to a number of solid-phase transformations and microstructural-evolution/rearrangement processes. It is, hence, not surprising that the overall mechanical (e.g., strength, toughness, ductility, etc.) and environmental resistance (e.g., corrosion resistance) properties of the weldments are greatly affected by the thermal histories of the material within the FZ and the HAZ.

In this study, microstructural-evolution in a GMAW butt weld of a prototypical (plain) low-carbon steel (AISI 1005) is analyzed computationally. In this type of steel, material within both the FZ and the HAZ undergoes a series of phase transformations during the GMAW process. Neglecting details regarding some of the low-temperature displacive/diffusionless phase transformations as well as details regarding the diffusion-controlled phase transformation produced microstructural constituents, the material within the FZ generally undergoes the following sequence of phase transformations: liquid $\rightarrow$ δ-ferrite $\rightarrow$ γ-austenite $\rightarrow$ α-ferrite, while material within the HAZ undergoes the following sequence of phase transformations: α-ferrite $\rightarrow$ γ-austenite $\rightarrow$ α-ferrite (Ref 2). It is generally recognized that: (a) the overall quality/soundness of the weld is controlled by the solidification process within the weld pool; while (b) the overall performance of the weldment is controlled by the portion of the material within the FZ or HAZ which is associated with the most inferior (thermal-history governed and material-system dependent) mechanical properties (Ref 6, 7). In the latter case, the thermal history affects the rate and the progress of various solid-state phase transformations as well as the material as-welded microstructure.

As mentioned above, in this study, development of the material microstructure within the FZ and the HAZ during GMAW in AISI 1005 butt welds will be studied computationally. Traditionally, evolution of the as-welded microstructure and the associated solid-state phase transformations are investigated experimentally using a variety of approaches, such as: (a) *Dilatometry* (Ref 8) a technique which relates dimensional changes in the test sample to the progress of the assumed/predicted phase transformations; (b) *spatially and time resolved x-ray diffraction* (Ref 2) a

synchrotron radiation-based technique which can not only monitor the progress but also identify the nature of the phase transformation(s); and (c) *post-mortem as-welded microstructure characterization* in this case, weldments are sectioned and examined using various microscopy, diffraction, scattering, and spectroscopy techniques. The results obtained are combined with the knowledge of the basic physical-metallurgy principles and the thermodynamics/kinetics phase transformations to infer the progress of phase transformation during GMAW.

As mentioned earlier, evolution of the FZ/HAZ material microstructure during GMAW is investigated in this study using computational methods and tools. Important inputs to this computational approach are the thermal history of the material points located at different portions of the FZ and the HAZ. Determination of these histories using a purely experimental approach(es) is quite challenging (if possible). Consequently, the thermal histories will be obtained in this study by carrying out a computational thermal analysis of the GMAW process.

1.3 Welding-Process Past Modeling Efforts

A comprehensive overview of the public-domain literature, carried out as part of this study, revealed several past efforts aimed at modeling the GMAW process. In general, the available GMAW-process models can be classified as: (a) models emphasizing heat transfer from the arc to the weld pool (Ref 9-11). In these types of models, thermal interaction of the arc with the stationary weld pool is analyzed, while mass transfer from the electrode to the weld pool via the process of molten-metal droplets generation and transfer is not considered; (b) combined heat and mass transfer GMAW-process models (Ref 12, 13). In this type of GMAW-process model, coupled heat/mass transfer analyses are utilized to account for the variety of the GMAW phenomena such as electrode-tip melting, droplet formation/detachment/transfer and impingement onto the weld-pool, dynamics of the weld pool and the interactions between the arc/plasma, molten-metal transfer, and the weld-pool surface; and (c) models focusing on the weld-pool heat/mass transfer and solidification processes and subsequent solid-state microstructure phase transformations and microstructural-evolution processes (Ref 2, 14). In this case, the weld pool is assumed to be subjected at the onset to a predefined temperature and velocity field and the heat/mass transfer analysis is combined with the basic physical-metallurgy principles to study the evolution of material microstructure during the welding process. The computational model developed in this study falls into this class of the GMAW-process models.

1.4 Main Objective

The main objective of this study is to develop a computational model which can be used to predict the distribution of the material microstructure in different FZ and HAZ locations of a GMAW butt weld produced under a given set of welding/process parameters. To reveal the details of the model, it will be applied to a prototypical (plain) low-carbon steel (AISI 1005). The results obtained will be compared with available open-literature experimental data to provide validation/verification for the proposed GMAW modeling effort.

1.5 Organization of the Article

A brief overview of the basic physical-metallurgy concepts and principles related to AISI 1005 and the associated family of plain low-carbon steels is provided in section 2. Details regarding the definition of the problems at hand, formulation of the corresponding mathematical models and the transient combined thermal-mechanical, finite-element analysis used are presented in section 3. The results pertaining to the spatial distribution of the final volume fractions of the key phases and microstructural constituents in the weld region of an AISI 1005 butt weld are presented and discussed in section 4. The main conclusions resulting from this study are summarized in section 5.

2. Basic Physical Metallurgy of AISI 1005

2.1 Chemical Composition and Phase Diagram

AISI 1005 is a (plain) low-carbon steel with the following nominal chemical composition expressed in wt.%: C—0.05, Mn—0.31, Si—0.18, Ni—0.11, Cr—0.10, P—0.009, Cu—0.008, S—0.005, Al—$<$0.005, Nb—$<$0.005, Mo—$<$0.005, Ti—$<$0.005, V—$<$0.005. To analyze the equilibrium state of this material at different temperatures (and under ambient atmospheric pressure), one should use the corresponding multi-component (equilibrium) phase diagram whose axes are the weight percentages of all the AISI 1005 main alloying elements (i.e., C, Mn, Si, Ni, etc.) and temperature. However, this is highly impractical due to the multi-dimensional nature of the phase diagram. Instead, one typically utilizes the so-called quasi-binary para-equilibrium Fe-C phase diagram. Such a phase diagram is alloy system dependent and is based on the assumption that the concentration of non-carbon alloying elements is the same in all the phases present and equal to that of the alloy system itself. In other words, it is assumed that due to their low diffusivity, partitioning of the non-carbon alloying elements between various phases does not take place. The quasi-binary para-equilibrium phase diagram of AISI 1005 is displayed in Fig. 2. Examination of this diagram reveals that it is quite similar to the true-binary Fe-C phase diagram except that the values of the characteristic concentrations and temperatures have been slightly changed. This is to be expected considering the fact that AISI 1005 is a (plain) low-carbon steel in which carbon dominates the thermodynamics of all the associated phase transformations.

2.2 Austenite Transformation(s) Within the FZ

2.2.1 Time-Temperature-Transformation (TTT) Austenite-Decomposition Diagram. As will be discussed later in greater detail, during cooling of the material within the FZ, austenite (a high-temperature γ-phase with face-centered-cubic, FCC crystal structure) undergoes transformation into a number of low-temperature ferrite (a low-temperature α-phase with body-centered-cubic, BCC crystal structure)-based phases/microconstituents. Some of these transformations are not predicted by the phase diagram as they occur under finite cooling-rate conditions and not under extremely slow/equilibrium cooling conditions. The first step towards investigating austenite-decomposition phase transformations under finite cooling rates is to construct and analyze the so-called TTT diagram for AISI 1005. In general, this diagram is experimentally constructed by quenching the steel in question from its fully austenitic region to a temperature below the austenite-transformation (also known as A_3) temperature and determining the so-called incubation time, i.e., the

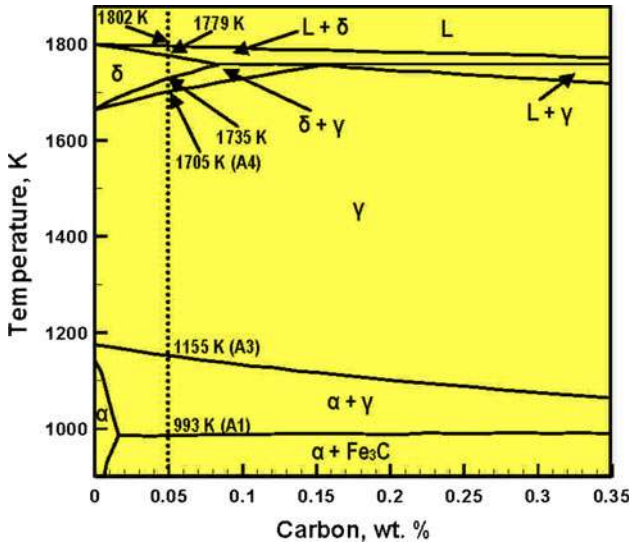

Fig. 2 A portion of the quasi-binary para-equilibrium Fe-C phase diagram corresponding to the non-carbon alloy additions at a level nominally found in AISI 1005 (Ref 36)

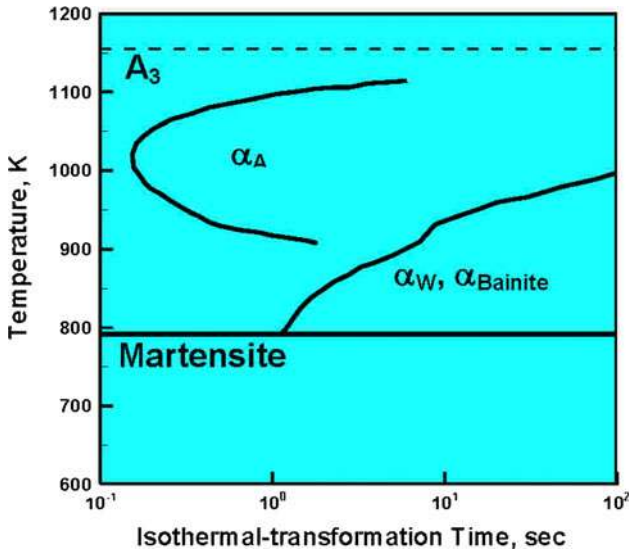

Fig. 3 The TTT diagram for AISI 1005 steel, showing the loci of time/temperature points associated with the transformation of austenite into allotriomorphic ferrite (α_A), Widmanstatten ferrite (α_w), bainite and/or martensite

time at which the phase transformation begins to occur (at the holding temperature). However, over the last 25 years major advances have been made in computational methods and tools for constructing the TTT diagrams non-experimentally by simply specifying the alloy chemical composition.

The TTT diagram for AISI 1005 is constructed, in this study, by following the procedure outlined in Ref 15 and previously employed in Ref 2. The result of this procedure is displayed in Fig. 3. Examination of the TTT diagram displayed in this figure reveals the presence of: (a) a high-temperature C-shaped curve which represents a locus of time/temperature points at which the replacive transformation of austenite into allotriomorphic ferrite (a variation of ferrite possessing a featureless external morphology which does not reflect the symmetry of the associated underlying crystalline structure) begins; (b) a low-temperature (upper half C-shaped) curve which corresponds to the displacive transformation of austenite into acicular/Widmanstatten ferrite (a version of ferrite possessing an acicular/lenticular-plate morphology which grows into the untransformed austenite from the austenite/austenite grain boundaries and/or allotriomorphic ferrite/austenite interfaces); and (c) a constant-temperature line denoting the highest temperature (the so-called martensite-start, M_S temperature) at which, during the initial quench, displacive/diffusionless austenite $\rightarrow$ martensite transformation takes place. For the two non-martensitic types of austenite-decomposition, Russell's formula (Ref 16, 17)

$$\tau = T^a \times (\Delta G_{\text{Max}})^b \times \exp\left(\frac{c}{T}\right) \times d \qquad \text{(Eq 1)}$$

is used to calculate the corresponding incubation time, τ, as a function of the maximum driving force for allotriomorphic ferrite nucleation, ΔG_{max}, and the associated rate-constants a, b, c, and d. The values of the required nucleation driving force, rate-constants and the M_S temperature are all obtained using the procedure outlined in Ref 15.

It should be noted that a constant-temperature line corresponding to the equilibrium austenite $\rightarrow$ allotriomorphic ferrite transformation (the so-called A_3-temperature) is also shown in Fig. 3. The value for the A_3-temperature (under the aforementioned para-equilibrium conditions) is also determined using the procedure outlined in Ref 15.

2.2.2 Continuous-Cooling-Transformation (CCT)Austenite-Decomposition Diagram. The TTT diagram was constructed under the unique thermal-history conditions within which austenite is quenched to a given temperature and then held at that temperature until the associated austenite-decomposition phase transformation begins to take place. Clearly, this is not a time history that a typical material point within the FZ will experience during its cooling to room temperature. Consequently, a procedure is needed that will enable determination of the start of the austenite-decomposition phase transformation under any thermal-history conditions. The procedure adopted in this study is based on the Scheil additive rule (Ref 18) as

$$\int_0^t \frac{\mathrm{d}t'}{\tau(T(t'))} = 1, \qquad \text{(Eq 2)}$$

where t is the (non-isothermal) incubation time associated with the cooling history $T(t')$, t' is a dummy-time variable and $t' = 0$ corresponds to the instance when the material point in question, during cooling, crosses the corresponding (i.e., $\gamma \rightarrow \alpha_{\text{allotriomorphic}}$ or $\gamma \rightarrow \alpha_{\text{Widmanstatten}}$) equilibrium transformation temperature. In the case of the austenite $\rightarrow$ allotriomorphic ferrite transformation, this temperature corresponds to the A_3 temperature, while in the case of the austenite $\rightarrow$ Widmanstatten ferrite this temperature can be operationally defined as the horizontal asymptote for the associated half C-shaped curve. The Scheil additive rule simply assumes that the material has to reach the same critical state of incubation for the transformation to proceed. The progress of the material towards this critical incubation state, at a given temperature T during cooling, is simply defined by the $\frac{\mathrm{d}t'}{\tau(T(t'))}$ ratio, and the time integral of this quantity at the onset of phase transformation, hence, has to be equal to 1.0.

The procedure described above is used to construct the CCT diagram for a series of austenite cooling histories, each associated with a constant cooling rate. The outcome of this procedure is displayed in Fig. 4. For improved clarity, the TTT curves are denoted in this figure using dashed lines. For the same reason, the resulting CCT curves are drawn as heavy, while representative cooling curves are denoted as light solid lines. It should be noted that, due to the athermal nature of the martensitic transformation, the M_S transformation temperature is not affected by the details of the material cooling history.

2.2.3 Phase Volume-Fraction Calculations. The TTT/CCT analyses presented above enable determination of the time/temperature condition at which, during cooling, austenite begins to transform into either the allotriomorphic or Widmanstatten ferrite. While this information is necessary, it is not sufficient relative to the main objective of this study which involves computational determination of the phase volume fractions. In addition, a complete analysis of the microstructural changes in the weld region must encompass both the FZ and the HAZ, while the TTT/CCT analyses were focused only on the microstructural changes within the FZ. In the remainder of this section, procedures are presented for computing the final volume fractions of the main phases/microstructural constituents within both the FZ and the HAZ.

2.2.4 Allotriomorphic Volume Fraction. Various experimental investigations have clearly revealed that growth of the allotriomorphic ferrite is greatly affected by the austenite grain structure, which, in turn, is greatly affected by details of the solidification process (Ref 2). Typically, in low-carbon steels, the as-cast microstructure, at high temperatures, consists of δ-ferrite. The δ-ferrite grains adjacent to the FZ/HAZ interface are equiaxed and very fine, forming the (quite thin) so-called chill zone. In the remainder of the FZ, the δ-ferrite grains are substantially coarser and columnar with their major axes being aligned with the direction of maximum heat extraction (Ref 19). During subsequent cooling, δ-ferrite → γ-austenite phase transformation takes place mainly through nucleation of the γ phase along the δ-ferrite grain boundaries and its growth in a direction normal to the grain boundaries. Consequently, austenite essentially inherits the δ-ferrite microstructure which is dominated by coarse columnar grains. For modeling purposes, the cross section of these grains is idealized as being of equal regular hexagonal shape. In other words, the columnar austenite grains are assumed to form a perfect honeycomb structure, as shown schematically in Fig. 5(a). It should be noted that the axis of the hexagonal prisms is aligned with the direction of maximum heat extraction. Also, it will be shown below that, within the γ-austenite → allotriomorphic ferrite growth model used in this study, the growth rate for allotriomorphic ferrite is affected by the austenite grain hexagonal cross section edge-length, a. The latter, in turn, is mainly affected by the maximum cooling rate attained by the melt at the FZ/HAZ interface during solidification. That is, the higher the cooling rate, the smaller the austenite grain transverse cross-sectional area (as quantified by a). No attempt was made in this study to model the solidification process accompanying GMAW and, hence, no functional relationship between the austenite grain size, a, and the GMAW-process parameters could be established. Instead, a prototypical value of $a = 47$ μm was used (Ref 20). In our future efforts, an attempt will be made to couple the present GMAW-process model with the type of GMAW-process model which emphasizes heat transfer from the arc and mass transfer from the electrode to the weld pool and, in turn, to investigate as-cast microstructural-evolution during the welding process.

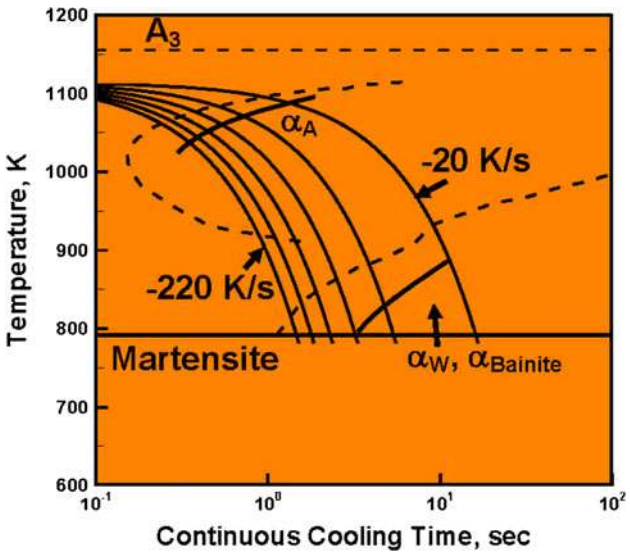

Fig. 4 Calculated CCT diagram for AISI 1005 steel: CCT curves and the M_s temperature line are denoted using heavy solid lines, while representative cooling curves are shown as light solid lines. The TTT curves and the A_3 temperature line are denoted using dashed lines

The allotriomorphic ferrite growth model utilized in this study assumes a parabolic relationship between the ferrite-thickness growth rate, $\frac{dq}{dt}$, and the instantaneous ferrite-plate thickness, q, as

$$\frac{dq}{dt} = \frac{\alpha_1(t)}{q}, \qquad \text{(Eq 3)}$$

where $a_1(t)$ is a one-dimensional temperature-dependent parabolic growth-rate constant.

Integration of Eq (3) between the time at which the growth starts, t_i, and the time at which the growth ceases, t_f, along the given temperature history, $T(t')$, yields the allotriomorphic ferrite finite-plate thickness, q_f, as

$$q_f = 0.5 \int_{t_i}^{t_f} \alpha_1(T(t'))t'^{-0.5}dt'. \qquad \text{(Eq 4)}$$

For any austenite cooling history, time t_i (and the associated γ-austenite → allotriomorphic ferrite phase transformation-start temperature) is obtained using the aforementioned CCT procedure and the upper TTT curve in Fig. 3. Likewise, t_f (and the associated γ-austenite → allotriomorphic ferrite phase transformation-end temperature) is determined using the same procedure, but with the lower TTT curve in Fig. 3. In other words, transformation of austenite into allotriomorphic ferrite is assumed to cease once kinetically superior austenite → Widmanstatten-ferrite transformation initiates. As far as the parabolic growth-rate constant is concerned, it is assumed to be controlled by carbon diffusion within austenite from the advancing allotriomorphic growth front. In other words, a para-equilibrium condition is assumed to prevail during the austenite → allotriomorphic ferrite transformation. This assumption is fully consistent with previous investigations (Ref 2). Temperature dependence of the parabolic

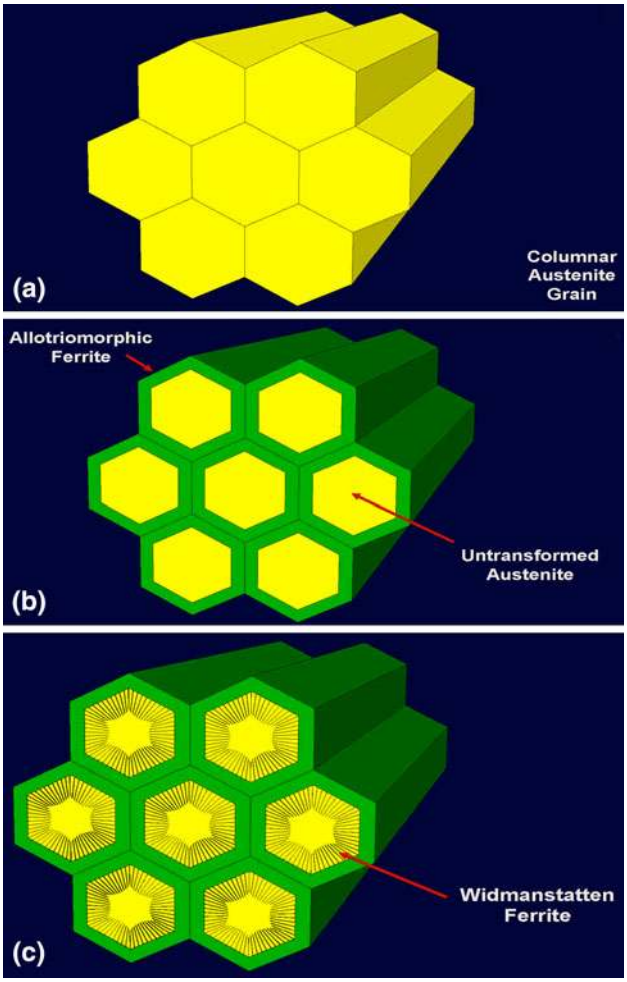

Fig. 5 Schematic representations of the columnar-grain microstructure in (a) untransformed austenite, (b) austenite partially transformed into allotriomorphic ferrite, and (c) austenite partially transformed into allotriomorphic and Widmanstatten ferrite

growth-rate constant, α_1, for AISI 1005 is depicted in Fig. 6 (Ref 20). It is seen that, as the temperature decreases, α_1 first increases as a result of an increased thermodynamic driving force for the austenite → allotriomorphic ferrite transformation. However, when the temperature becomes sufficiently low, the associated reduced carbon diffusivity begins to control the overall rate of this transformation leading to a reduction in α_1.

Using simple geometrical arguments and the schematic displayed in Fig. 5(b), pertaining to a partially transformed section of austenite, a functional relationship can be established between the allotriomorphic ferrite-plate thickness, q_f, and its volume fraction, $V_{\alpha A}$, as

$$V_{\alpha A} = \frac{[2q_f \tan(30^\circ)(2a - 2q_f \tan(30^\circ))]}{a^2}. \quad \text{(Eq 5)}$$

2.2.5 Widmanstatten Volume Fraction. As mentioned above, the onset of austenite to Widmanstatten-ferrite phase transformation causes the kinetically more sluggish austenite to allotriomorphic ferrite transformation to cease. The growth rate of the Widmanstatten ferrite is assumed, in this study, to be controlled by the rate of lengthening of this lens-shaped phase in a direction normal to the local allotriomorphic ferrite/

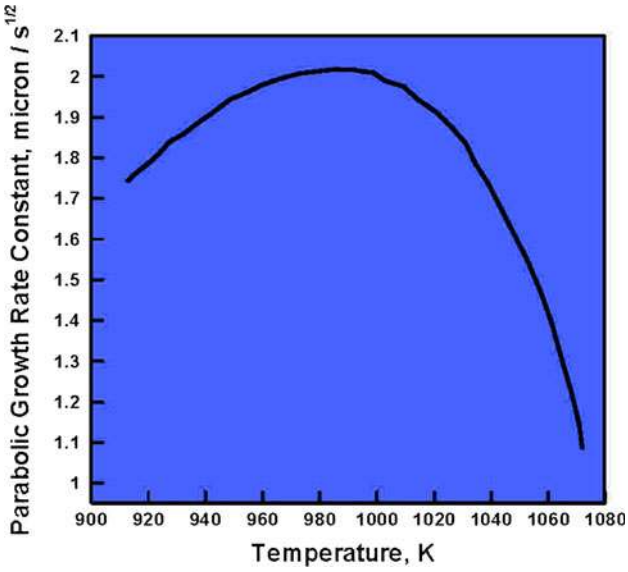

Fig. 6 Temperature dependence of the one-dimensional parabolic growth-rate constant for the austenite → allotriomorphic ferrite phase transformation in AISI 1005 (Ref 20)

austenite interface. A schematic of partially transformed austenite grains containing prior grain-boundary regions transformed into allotriomorphic ferrite and lenticular-shaped Widmanstatten plates advancing from the allotriomorphic ferrite/austenite interfaces toward the grain centers is depicted in Fig. 5(c). While this rate is affected by the para-equilibrium condition still present at the ferrite advancing front and the associated carbon diffusion from this front into the untransformed austenite, the displacive character of the austenite to Widmanstatten-ferrite transformation also plays an important role in the kinetics of this transformation (Ref 5, 21). Following the procedure described in Ref 5, 21 which is based on the calculation of the Widmanstatten-ferrite area fraction within the hexagonal-shaped austenite grains, Fig. 5(c), the following expression is used for determining the Widmanstatten-ferrite volume fraction, $V_{\alpha W}$

$$V_{\alpha W} = C_4 G \left[\frac{2a - 4q_f \tan(30^\circ) t_{\alpha W}^2}{(2a)^2}\right], \quad \text{(Eq 6)}$$

where C_4 (=7.367 s^{-1}, Ref 20) is an alloy-composition independent constant, G (=52 μm/s, Ref 20) is the Widmanstatten-ferrite lengthening rate, and $t_{\alpha W}$ is the total time available for the austenite to Widmanstatten-ferrite transformation (it should be recalled that once temperature drops below M_S, the austenite to Widmanstatten-ferrite transformation ceases and it is replaced with an athermal martensitic transformation).

2.2.6 Volume Fraction of Other Microconstituents Resulting from Austenite Transformation. In addition to allotriomorphic and Widmanstatten ferrite, the room-temperature FZ as-cast microstructure may also contain other phases/microconstituents, primarily bainite, martensite and retained austenite. As it is generally difficult to make a clear distinction between Widmanstatten ferrite and bainite, austenite to bainite phase transformation is not modeled explicitly, and it is simply lumped with the austenite to Widmanstatten-ferrite transformation. Hence, no separate volume fraction of bainite is calculated within the present procedure. As far as retained austenite is

concerned, its volume fraction in AISI 1005 is typically very small and, hence, it is assumed to be zero in this study. Thus, the only remaining major phase/microconstituent which could be found in the AISI 1005 room-temperature FZ as-cast microstructure is martensite, and its volume fraction V_{M_s} can be simply computed as

$$V_{M_s} = 1 - V_{\alpha A} - V_{\alpha W}. \quad \text{(Eq 7)}$$

2.3 Phase Transformations within the HAZ

2.3.1 Ferrite to Austenite Transformation During Heating. While the material within the FZ undergoes, during GMAW, cooling from its deposition temperature to room temperature, the material within the HAZ initially experiences heating and then subsequent cooling. The HAZ is operationally defined as a region surrounding the FZ within which thermal cycling described above causes noticeable and significant changes in the weldment-material microstructure and properties. It should be noted that the material within the workpiece components to be welded can have a variety of as-received microstructures depending on the prior thermal-mechanical history of the material. While details of various such microstructures can have some effect on the extent of microstructural changes in the HAZ, these details are beyond the scope of this study. Instead, the as-received workpiece-material microstructure is assumed to be fully ferritic (simply stated, allotriomorphic ferrite, Widmanstatten ferrite, bainite and martensite are all considered as different renditions of the same crystalline phase, ferrite). The main microstructure changes in the HAZ during the heating portion of the thermal cycle are associated with a ferrite to austenite transformation, while during cooling austenite transforms back into one or more phases/constituents, in accordance with the thermodynamics and kinetics relations provided in the previous section.

In AISI 1005, as in most low-carbon steels, ferrite to austenite transformation involves nucleation of austenite and its subsequent carbon-diffusion-controlled growth (under para-equilibrium conditions, assumed in this study). Consequently, the progress of this transformation is generally represented using the so-called Kolmogorov-Johnson-Mehl-Avrami (KJMA) relation (Ref 22). In the case of an isothermal ferrite to austenite phase transformation, the KJMA relation can be expressed as

$$V_\gamma = 1 - \exp[-\{k(T) \times t\}^n], \quad \text{(Eq 8)}$$

where V_γ represents the austenite volume fraction, $k(T)$ is a nucleation/growth-rate-related kinetic parameter, t is the isothermal-holding time at temperature T, and n (=1.9, Ref 2) is a temperature-invariant exponent. Temperature dependence of k is normally defined using an Arrhenius-type relation in the form

$$k(T) = k_0 \times \exp\left(-\frac{Q}{RT}\right), \quad \text{(Eq 9)}$$

where k_0 (=1.33×10^5 s^{-1}, Ref 2) is a pre-exponential constant, Q (=117.07 kJ/mol, Ref 2) is an overall nucleation/growth activation energy for the ferrite to austenite phase transformation while R is the universal gas constant. It should be noted that the KJMA model parameters k_0, Q and n are normally obtained using multiple-regression of the isothermal-kinetics experimental data.

Equation (8) cannot be directly used in the analysis of the ferrite to austenite phase transformation within the HAZ, as this transformation proceeds under continuous heating rather than under isothermal-holding conditions. Instead, one should first approximate a $T(t)$ continuous heating function, as a sequence of N isothermal-holding steps each associated with a temperature T_i (i = 1, 2,…,N) and of a duration Δt. Then Eq (8) could be modified to account for the cumulative contribution of all the isothermal-transformation steps as

$$V_\gamma(t(T_N)) = 1 - \exp\left[-\left\{\sum_{i=1}^{N} k(T_i) \times \Delta t\right\}^n\right] = 1 - \exp\left[-\left\{\sum_{i=1}^{N} k_0 \times \exp\left(-\frac{Q}{RT_i}\right) \times \Delta t\right\}^n\right]. \quad \text{(Eq 10)}$$

2.3.2 Austenite Transformation During Cooling. The austenite formed within the HAZ during heating transforms back to ferrite during subsequent cooling of this weld region to room temperature. As the HAZ microstructure at the peak temperature contains ferrite/austenite interfaces, the austenite → ferrite transformation is assumed to involve only the carbon-diffusion-controlled growth of the existing ferrite plates (and not the ferrite nucleation process). Consequently, the progress of the ferrite → austenite transformation during cooling within the HAZ is assumed to be given by the same kinetic relations as those defined in the previous section.

3. Computational Procedure

Modeling of the GMAW process carried out in this study employs a modified version of the transient fully coupled thermomechanical finite-element procedure which was developed in our prior work dealing with friction stir welding (FSW) (Ref 23-31). As a detailed account of the procedure was provided in Ref 31, only a brief overview of the features unique to the GMAW process will be presented in the remainder of this section.

3.1 Geometrical Model

The computational domain used consists of a (120 × 60-240 × 15 mm) rectangular parallelepiped with the parallelepiped axis aligned with the global Cartesian x-y-z coordinate system, Fig. 7(a). The parallelepiped is oriented in such a way that the weld contact interface is orthogonal to the x-axis, weld gun travel direction is along the y-axis, while the workpiece upward normal is along the z-axis. The coordinate system origin is placed at the center (x = 0)/front (y_{min} = 0)/bottom (z = 0) point of the computational domain. A V-shaped through-the-thickness section centered at x = 0 and running along the y-axis is created initially by removing the associated workpiece material, and the removed material is added, in a gradual manner, to mimic groove filling in the spray mode during the GMAW process. In addition, the geometry of the restored material has been changed to form a dome-shaped weld top, Fig. 7(a). It should be noted that the computational domain described above possesses a symmetry plane at x = 0 and, hence, only one (left) half of this computational domain is explicitly analyzed in this study.

3.2 Meshed Model

The selected half of the computational domain is meshed using between 54,000 and 216,000 first-order eight-node reduced-integration hexahedral thermomechanically coupled solid elements. A close-up of the typical meshed model used in this study is shown in Fig. 7(b).

3.3 Computational Algorithm

As mentioned above, the GMAW process is analyzed computationally using a transient fully coupled, thermomechanical, unconditionally stable, implicit finite-element algorithm within which the "V-grooved" workpiece components are supported from the bottom, made stress-free and initially placed at the ambient temperature, while a high-temperature welding/filler material is gradually replaced within the groove. Three basic heat transfer modes, conduction, convection and radiation, are activated while non-uniformity in the temperature spatial distribution is allowed to produce thermal stresses which, if sufficiently high, could induce plastic deformation and residual stresses. To account for the fact that a small fraction of the plastic-deformation work is stored in the form of crystalline defects, 95% of this work was arbitrarily assumed to be dissipated in the form of heat.

3.4 Initial Conditions

As mentioned above, the workpiece and the welding/filler material are initially assumed to be stress-free but at different temperatures, i.e., (a) the workpiece material is assumed to be at the ambient temperature; while (b) the welding/filler material is assumed to be at a temperature which exceeds the material liquidus temperature. No attempt was made in this rendition of the GMAW-process model to relate this temperature to the basic welding-process parameters. This will be done in our future efforts, which will include coupling of the present GMAW-process model with the type of GMAW-process model which emphasizes heat transfer from the arc, and mass transfer from the electrode, to the weld pool.

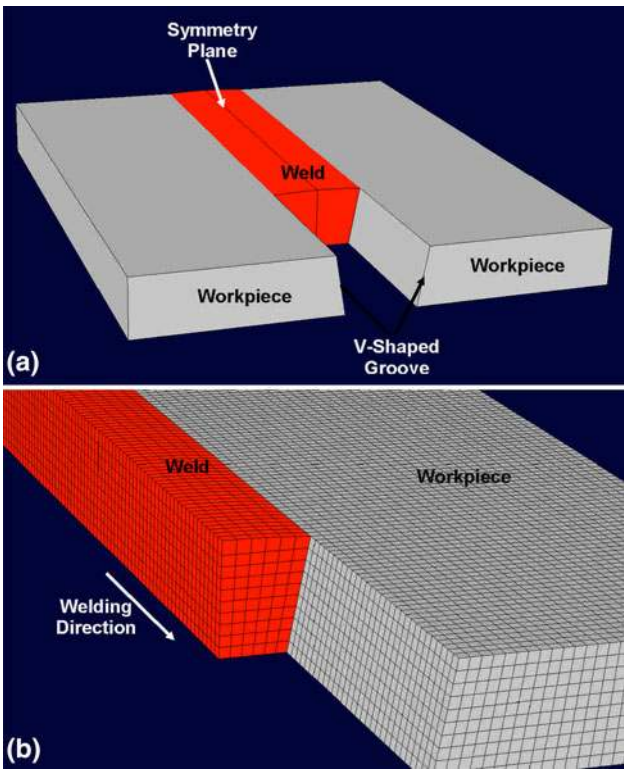

Fig. 7 Typical (a) geometrical and (b) meshed models used in the present analysis of the GMAW process

3.5 Boundary Conditions

As the computational domain explicitly analyzed represents only one half of the workpiece/weld assembly, symmetry mechanical and thermal boundary conditions are applied across the $x = 0$ symmetry plane. As mentioned above, the "V-grooved" workpiece components are supported from the bottom and no other mechanical boundary conditions are utilized/prescribed. As far as the thermal boundary conditions are concerned, natural-convection and radiation boundary conditions are prescribed over all external surfaces of the workpiece/weld.

3.6 Mesh Sensitivity

In order to ensure that the key results and conclusions yielded by this study are not affected by the choice of the computational mesh, a mesh sensitivity analysis was carried out involving the use of progressively finer finite-element meshes. The finite-element mesh finally selected is a compromise between the computational efficiency and the numerical accuracy.

3.7 Material Model

It should be noted that the finite-element-based computational procedure described above was used in this study mainly to generate thermal histories of the material points within the FZ and the HAZ. In other words, no allowance was given within this analysis for the occurrence of various phase transformations accompanying material cooling within the FZ and the material heating/cooling within the HAZ. However, these transformations will be investigated, in section 4, for the obtained cooling histories, in a post-processing analysis which utilized the TTT/CCT procedures developed in section 2.

Based on the description provided above, it is evident that the material utilized within the finite-element analysis was assumed to be homogeneous, single-phase and non-transforming/stable. In addition, the workpiece components and the welding/filler material are assumed to be represented by an identical material thermal-mechanical model. The mechanical portion of the workpiece/weld-material response is assumed to be isotropic, linear-elastic and strain-hardenable, strain-rate sensitive, thermally softenable plastic and that it can be represented using the Johnson-Cook material-model formulation (Ref 32).

Within this model, the purely elastic response of the material is defined using the generalized Hooke's law. On the other hand, the elastic/plastic response of the material is described using the following three relations: (a) a *yield criterion*, i.e., a mathematical relation which defines the condition which must be satisfied for the onset (and continuation) of plastic deformation; (b) a *flow rule*, i.e., a relation which describes the rate of change of different plastic-strain components during plastic deformation; and (c) a *constitutive law*, i.e., a relation which describes how the material-strength changes as a function of the extent of plastic deformation, the rate of deformation and temperature.

Table 1 Johnson-Cook strength model material parameters for AISI 1005

Parameter	Symbol	Units	Value
Young's Modulus	E	GPa	205-215
Poisson's ratio	ν	N/A	0.285-0.295
Reference strength	A	MPa	310.0
Strain-hardening Parameter	B	MPa	350.0
Strain-hardening exponent	n	N/A	0.3
Strain-rate coefficient	C	N/A	0.02
Room temperature	T_{room}	K	298.0
Melting temperature	T_{melt}	K	1492-1526
Temperature exponent	m	N/A	0.5

Table 2 General, thermomechanical, and thermal parameters for AISI 1005

Parameter	Symbol	Units	Value
Material mass density	ρ	kg/m^3	7800-7900
Coefficient of linear thermal expansion	α	1/K	1.15e−5-1.3e−5
Specific heat	C_p	$\text{J/kg} \cdot \text{K}$	465-505
Thermal conductivity	k	$\text{W/m} \cdot \text{K}$	50-54
Heat transfer coefficient	h	$\text{W/m}^2 \cdot \text{K}$	40-50
Sink temperature	T_{sink}	K	298
Emissivity	ε	N/A	0.77
Ambient temperature	T_{amb}	K	298

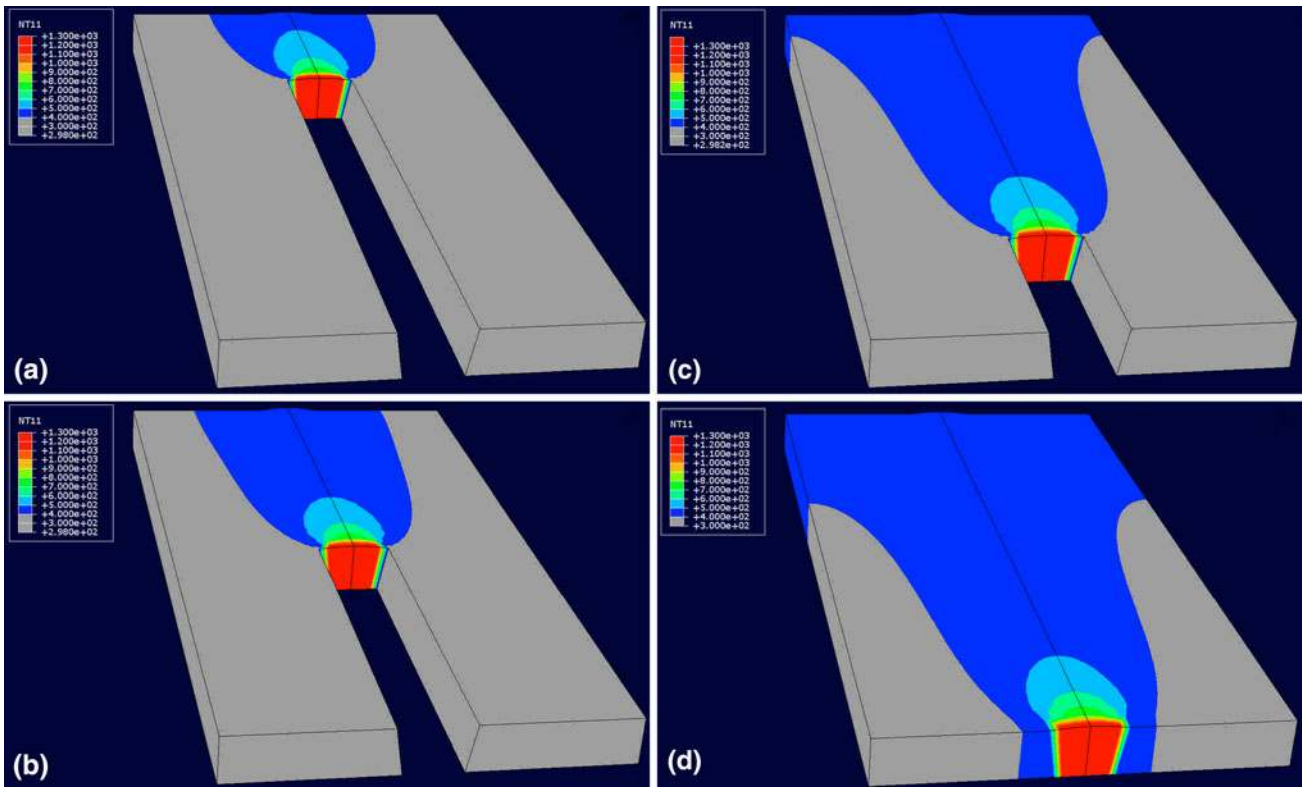

Fig. 8 An example of typical results pertaining to the spatial distribution and temporal evolution of temperature in the weld region at relative welding times of (a) 0 s, (b) 10 s, (c) 20 s, and (d) 30 s

For AISI 1005, as for the most metallic materials, plasticity is considered to be of a purely distortional (volume-preserving) character and the yield criterion and the flow rule are, respectively, defined using the von Mises yield criterion and a normality flow rule. The von Misses yield criterion states that equivalent stress (a scalar, frame-invariant function of the deviatoric stress components) must be equal to the material yield strength for plastic deformation to occur/proceed. The

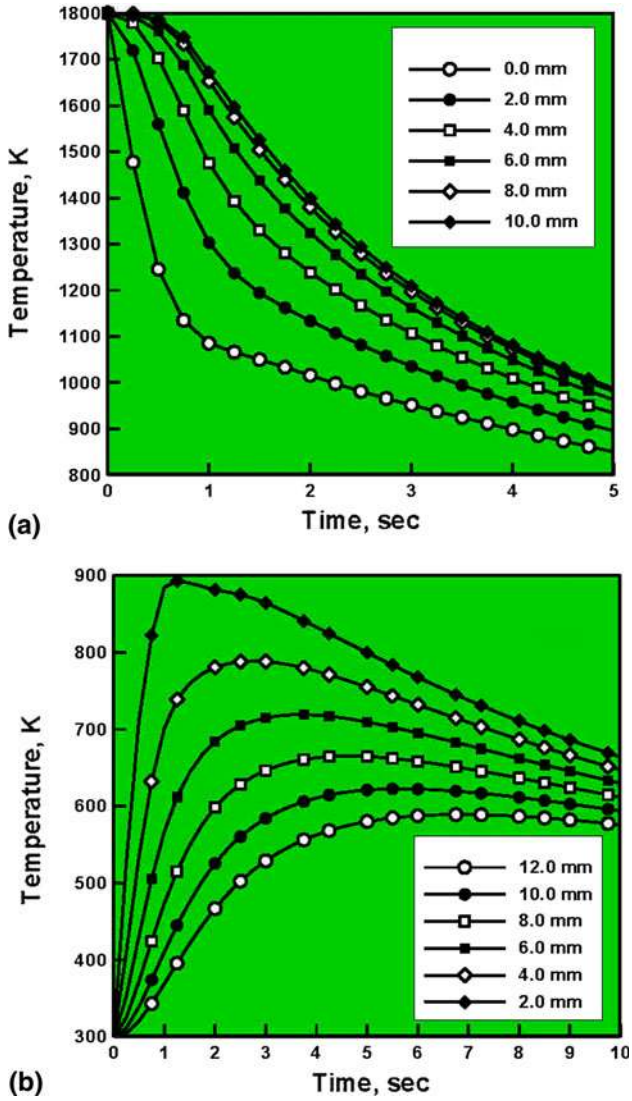

Fig. 9 An example of typical results pertaining to the temporal evolution of temperature (a) along the workpiece mid-plane within the FZ (the labels used represent the distance of the material point in question from the weld *yz*-symmetry plane) and (b) along the workpiece mid-plane within the heat-affected zone, HAZ (the labels used represent the distance of the material point in question from the HAZ/FZ interface)

normality flow-rule states that the plastic flow takes place in the direction of the stress-gradient of the yield surface (a locus of the stress/strain points within the associated multi-dimensional space at which the von Mises stress criterion is satisfied). The Johnson-Cook strength constitutive law is defined as

$$\sigma_y = A\left[1+\frac{B}{A}\left(\bar{\varepsilon}^{\mathrm{pl}}\right)^n\right]\left[1+C\log\left(\dot{\bar{\varepsilon}}^{\mathrm{pl}}/\dot{\bar{\varepsilon}}_0^{\mathrm{pl}}\right)\right]\left[1-T_{\mathrm{H}}^m\right], \quad \text{(Eq 11)}$$

where $\bar{\varepsilon}^{\mathrm{pl}}$ is the equivalent plastic strain, $\dot{\bar{\varepsilon}}^{\mathrm{pl}}$ the equivalent plastic strain rate, $\dot{\bar{\varepsilon}}_0^{\mathrm{pl}}$ a reference equivalent plastic strain rate, A the zero plastic strain, unit plastic strain rate, room-temperature yield strength, B the strain-hardening constant, n the strain- hardening exponent, C the strain-rate constant, m the thermal-softening exponent and $T_{\mathrm{H}} = (T - T_{\mathrm{room}})/(T_{\mathrm{melt}} - T_{\mathrm{room}})$ a room-temperature (T_{room})-based homologous temperature while T_{melt} is the melting (or more precisely, solidus) temperature. All temperatures are given in Kelvin. In Eq (11), the parameter A defines the as-annealed material yield strength, the term within the first pair of brackets defines the effect of strain hardening, the term within the second pair of brackets quantifies the effect of deformation rate, while the last term shows the reversible effect of temperature.

The thermal-portion of the material model is defined using the: (a) material mass density, ρ, specific heat, C_{p}, and thermal conductivity, k, for the heat-conduction part of the model; (b) the heat transfer coefficient, h, and the sink temperature, $T_{\mathrm{sink}} = T_{\mathrm{room}}$, for the natural-convection part of the model; and (c) emissivity, ε, and the ambient temperature, $T_{\mathrm{amb}} = T_{\mathrm{room}}$, for the radiation part of the model.

A summary of the values for all the AISI 1005 thermal-mechanical model parameters used in this study is provided in Tables 1 and 2.

3.8 Computational Tool

The transient fully coupled thermomechanical problem dealing with GMAW, as described above, is solved using an implicit solution algorithm implemented in ABAQUS/Standard (Ref 33), a general purpose finite-element solver. In addition, Matlab (Ref 34), a general purpose mathematical package was used to automate ABAQUS input file construction, as progressive replacement of the welding/filler material required using a large number of computational steps involving mesh models with a continuously increasing number of elements.

4. Results and Discussion

In this section, typical results obtained using the present transient fully coupled, thermal-mechanical analysis of the GMAW process are presented and discussed. Some of these results (such as the ones pertaining to the spatial distribution of the equivalent plastic strain and the residual von Mises stress in the weldment) are presented to merely demonstrate the capabilities of the present analysis. However, these results were not used in the current rendition of the microstructural-evolution and phase volume-fraction computational procedure. On the other hand, detailed results pertaining to the temperature history of the characteristic material points within the FZ and the HAZ are used in the analyses of microstructural-evolution and during the calculations of the phase volume fractions.

4.1 Typical Results

4.1.1 Spatial Distribution and Temporal Evolution of Temperature. An example of typical results pertaining to the spatial distribution and temporal evolution of temperature in the weld region are presented in Fig. 8(a) to (d). The results displayed in these figures are obtained at relative welding times of 0, 10, 20, and 30 s, respectively. For improved clarity, the workpiece portions residing on the ambient (298 K) temperature are shown as light gray regions. Examination of the results displayed in Fig. 8(a) to (d) clearly reveals that: (a) deposition of the high-temperature filler material into the groove causes an instantaneous increase in temperature in the adjacent region of the workpiece/weld; (b) as welding proceeds, previously deposited filler material cools by losing its heat through natural convection and radiation to the surroundings and by conduction

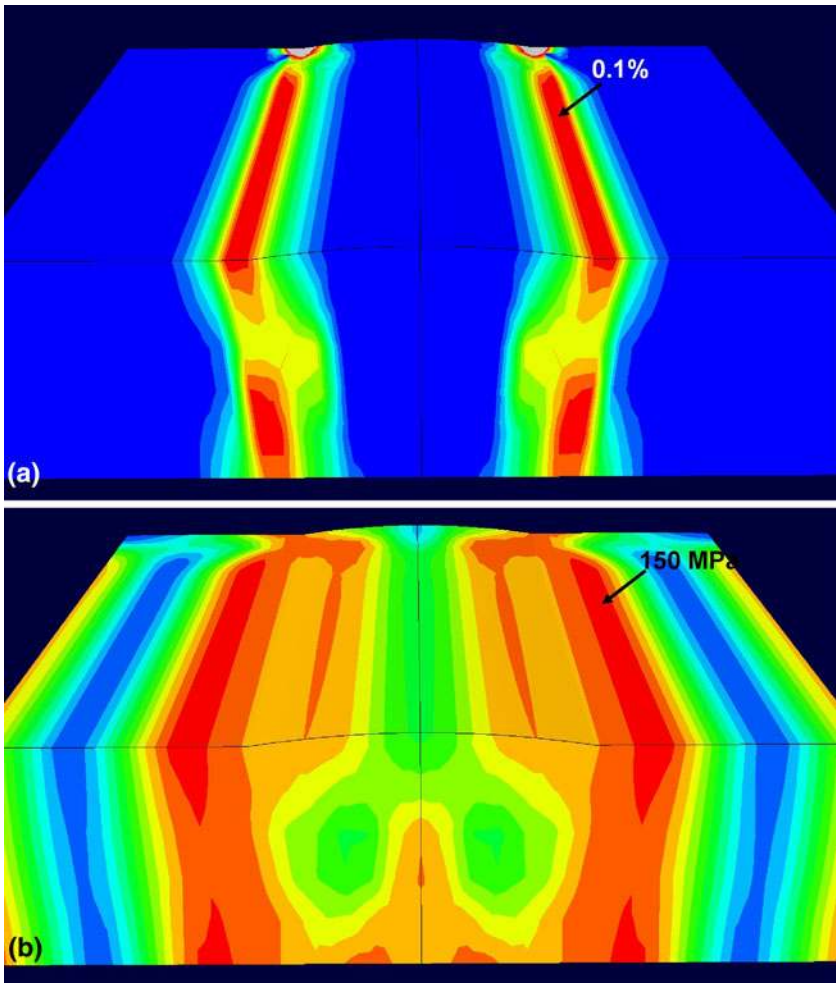

Fig. 10 An example of typical results pertaining to the spatial distribution of (a) equivalent plastic strain and (b) residual von Mises equivalent stress over a transverse section of the weld and the workpeice region adjacent to the weld

through the adjacent workpiece-material region; and (c) propagation of the thermal-conduction wave within the workpiece can be clearly observed by monitoring the expansion of the 400 K temperature contour over the workpiece top surface.

4.1.2 Thermal History of the FZ and HAZ. Typical results pertaining to the thermal history of the material points lying on the workpiece mid-plane during the GMAW process are displayed in Fig. 9(a) and (b). The results displayed in Fig. 9(a) are obtained within the FZ and the curve labels used represent the distance of the material point in question from the weld *yz*-symmetry plane, while the results displayed in Fig. 9(b) show the corresponding HAZ results where the curve labels used, in this case, represent the distance of the material point in question from the HAZ/FZ interface. It should be noted that the results, such as those displayed in Fig. 9(a) and (b), but for a substantially larger number of material points, will be used in the next section to determine the phase volume fractions in the weld region. Examination of the results displayed in these figures reveals that: (a) material points within the FZ undergo continuous cooling; (b) the initial cooling rate is highest for the FZ material points which are closest to the workpiece/weld interface; (c) as far as material points within the HAZ are concerned, as expected, they experience a complex heating-cooling thermal history; and (d) material points within the HAZ which are closest to the workpiece/weld interface experience the maximum temperature during the GMAW process.

4.1.3 Plasticity and Residual Stresses. As mentioned earlier, large temperature gradient-induced thermal stresses in the weld region combined with the attendant thermally softened workpiece/weld material(s), can lead, during the GMAW process, to plastic deformations, and during the subsequent cooling to room temperature, to the development of residual stresses. An example of the typical results obtained in this portion of the work is displayed in Fig. 10(a) and (b). For improved clarity, contour-level legends are not displayed, but instead, the maximum values of the equivalent plastic strain and the von Mises residual stress are denoted in Fig. 10(a) and (b), respectively. Examination of the results displayed in these figures reveals that, as expected, the largest plasticity/residual stress effects are observed in the regions surrounding the HAZ/FZ interface. It should be noted that the displacive-type austenite-ferrite transformations are expected to be affected by both plastic strains and the residual stresses through the so-called deformation-induced and stress-assisted effects (Ref 35, 37, 38). However, inclusion of these phenomena is beyond the scope of this study, but will be addressed in our future efforts.

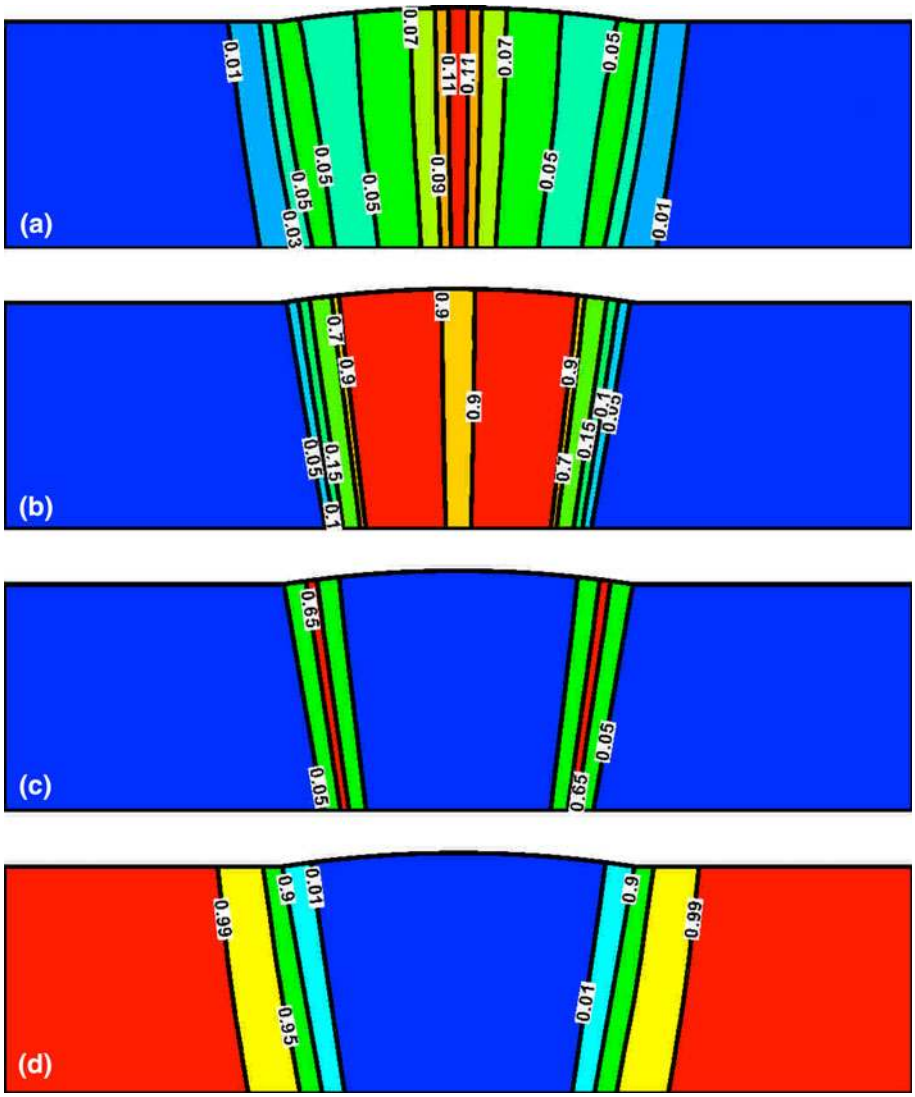

Fig. 11 An example of typical results pertaining to the spatial distribution of phase volume fraction for (a) allotriomorphic ferrite, (b) Widmanstatten ferrite, (c) martensite, and (d) normalized ferrite over a transverse section of the weld and the workpeice region adjacent to the weld

4.2 Prediction of the Room-Temperature Weld Microstructure

The thermal history results like the ones reported in the previous section, Fig. 9(a) and (b), is used as input to the FZ and HAZ microstructural-evolution analysis presented in section 2 to determine the final volume fractions of different crystalline phases in the weld region. The microstructural-evolution analysis presented in section 2 revealed that the nature of the phase transformations encountered and their thermodynamic/kinetic relations are drastically different for the material points residing in the FZ and in the HAZ. Consequently, different microstructural-evolution functional relationships had to be applied to the material points residing in these two portions of the weld region. Once these relations have yielded the results pertaining to the spatial variation of the phase volume fraction within the FZ and the HAZ, the results are combined to generate phase volume-fraction contour plots, one contour plot for each crystalline phase analyzed. In this analysis, it was assumed that the as-received AISI 1005 was in a normalized (heat-treatment) condition and that its microstructure consists fully of "normalized" ferrite. Based on this assumption, and considering details of the analysis presented in section 2, any portion of the weld region can contain up to four crystalline-phase/microconstituents: (a) allotriomorphic ferrite; (b) Widmanstatten ferrite; (c) martensite; and (d) normalized ferrite.

An example of the results obtained using the aforementioned procedure is depicted in Fig. 11(a) to (d). These figures display, respectively, the spatial distribution of phase volume fraction for: (a) allotriomorphic ferrite; (b) Widmanstatten ferrite; (c) martensite; and (d) normalized ferrite over a transverse section of the weld and the workpiece region adjacent to the weld. Examination of the results displayed in Figs. 11(a) to (d) revealed that:

(a) The allotriomorphic ferrite volume fraction takes on the largest value along the weld *xz*-symmetry plane, Fig. 11(a). This finding is consistent with the fact that the average cooling rate in this region is the smallest, Fig. 9(a)

(b) As the distance from the weld *xz*-symmetry plane increases, the allotriomorphic ferrite volume fraction decreases in a fairly monotonic fashion (until the FZ/HAZ interface is reached), Fig. 11(a). As one enters the HAZ from the FZ, slightly higher values of the allotriomorphic ferrite volume fraction are encountered, Fig. 11(a), indicating that, in this region, a significant extent of the normalized ferrite → austenite transformation was attained. As one moves towards the base-metal/HAZ interface, this volume fraction monotonically decreases and ultimately becomes zero, Fig. 11(a). This demonstrates that, as expected, no normalized ferrite → austenite transformation takes place in the base-metal.

(c) The Widmanstatten-ferrite volume fraction within the FZ initially increases with the distance from the weld *xz*-symmetry plane, Fig. 11(b). This finding is fully consistent with the fact that the associated average cooling rate also increases. However, near the FZ/HAZ interface, the cooling rate becomes sufficiently high to kinetically inhibit the progress of the austenite → Widmanstatten-ferrite transformation and to promote formation of martensite. Consequently, this region of the FZ contains a lower volume fraction of the Widmanstatten ferrite, Fig. 11(b) and a substantial volume fraction of the martensitic phase, Fig. 11(c).

(d) As expected, material within the FZ which was initially in the molten state does not contain any normalized ferrite, Fig. 11(d). At the FZ/HAZ boundary, the normalized ferrite volume fraction jumps to a value slightly lower than 1.0. As one approaches the base-metal/HAZ interface within the HAZ, this volume fraction monotonically increases towards 1.0, Fig. 11(d). The locus of the points at which this volume fraction acquires a value of 1.0 constitutes the base-metal/HAZ interface.

4.3 Model Validation

The analysis of the results pertaining to the spatial distribution of different crystalline phases and microstructural constituents within the weld region presented in the previous section established that the model predictions are in good qualitative agreement with their experimental counterparts. Unfortunately, quantitative validation of the present model cannot be carried out for a number of reasons: (a) the present model does not enable determination of the effect of the GMAW-process parameters on the weld-material microstructure spatial distribution. Namely, the present model uses the weld-pool temperature as an initial condition and is not capable of relating this temperature to the GMAW-process parameters. As was mentioned earlier, this deficiency of the current model will be addressed in our future work; (b) as part of a larger-scale effort dealing with the problem of computationally assisted development of the GMAW process and high-performance weldments, GMAW experimental facilities are currently being developed/assembled. These facilities have not yet yielded results which can be used to help quantitatively validate the present model; and (c) no open-literature experimental results pertaining to the spatial distribution of various crystalline phases and microstructures within the AISI 1005 weld region could be found.

To temporarily overcome the problem of insufficient validation of the present model, the microstructural evolution model within the FZ is combined with the cooling-rate results obtained in Ref 2 for the case of the Gas Tungsten Arc Welding (GTAW) of AISI 1005 steel and compared with the experimental results reported in the same reference. The present model predictions and the experimental results reported in Ref 2 are found to be in reasonably good agreement.

5. Summary and Conclusions

Based on the work presented and discussed in this study, the following main summary remarks and conclusions can be made:

1. A conventional GMAW butt-joining process is analyzed computationally using a fully coupled, transient, thermal-mechanical finite-element procedure within which thermal-mechanical coupling is attained by accounting for the temperature dependence of the workpiece-material mechanical model and by treating the plastic deformation as a potential heat source in the heat-conduction equation.
2. The finite-element procedure is subsequently combined with the basic physical-metallurgy concepts and principles to model microstructural-evolution within the weld FZ and weld HAZ.
3. To demonstrate the utility of the present approach, the procedure is applied to a prototypical (plain) low-carbon steel (AISI 1005). Detailed examination of the predicted spatial distribution of the volume fractions of various crystalline phases and microconstituents established that these are in good qualitative agreement with general experimental observations/findings reported in the open literature.
4. Issues related to a more quantitative validation of the present model as well as those related to the future improvements in the model are also discussed.

Acknowledgments

The material presented in this paper is based on work supported by two Army Research Office sponsored grants (W911NF-11-1-0207 and W911NF-09-1-0513) and two US Army/Clemson University Cooperative Agreements (W911NF-04-2-0024 and W911NF-06-2-0042). The authors are indebted to Dr. Larry C. Russell, Jr. of ARO for his continuing support and interest in this study.

References

1. A.D. Althouse, C.H. Turnquist, W.A. Bowditch, K.E. Bowditch, and M.A. Bowditch, Gas Metal Arc Welding, *Modern Welding*, 10th ed., Goodheart-Willcox Publisher, Tinley Park, IL, 2004, p 233–265
2. W. Zhang, J.W. Elmer, and T. DebRoy, Modeling and Real Time Mapping of Phases During GTA Welding of 1005 Steel, *Mater. Sci. Eng., A*, 2002, **333**, p 320–335
3. Ø. Grong, *Metallurgical Modelling of Welding*, 2nd ed., The Institute of Materials, London, 1997
4. K. Easterling, *Introduction to the Physical Metallurgy of Welding*, 2nd ed., Butterworth Heinemann, Boston, 1992
5. L.-E. Svensson, *Control of Microstructures and Properties in Steel Arc Welds*, CRC Press, Boca Raton, 1994

6. R. Mancini and C. Budde, Reaustenitisation in Fe-C Steels Revisited, *Acta Mater.*, 1999, **47**, p 2907–2911
7. R.C. Reed, T. Akbay, Z. Shen, J.M. Robinson, and J.H. Root, Determination of Reaustenitisation Kinetics in a Fe-0.4C Steel Using Dilatometry and Neutron Diffraction, *Mater. Sci. Eng., A*, 1998, **256**, p 152–165
8. J.H. Valentich, *Tube Type Dilatometers: Applications from Cryogenic to Elevated Temperatures Instrument Society of America*, Research Triangle Park, Research Triangle Park, NC, 1981
9. J. Haidar, A Theoretical Model for Gas Metal Arc Welding and Gas Tungsten Arc Welding. I, *J. Appl. Phys.*, 1998, **84**, p 3518–3529
10. J. Haidar, Prediction of Metal Droplet Formation in Gas Metal Arc Welding. II, *J. Appl. Phys.*, 1998, **84**, p 3530–3540
11. J. Haidar, An Analysis of Heat Transfer and Fume Production in Gas Metal Arc Welding. III, *J. Appl. Phys.*, 1998, **85**, p 3448–3459
12. J. Hu and H.L. Tsai, Heat and Mass Transfer in Gas Metal Arc Welding. Part I: The Arc, *Int. J. Heat Mass Transf.*, 2007, **50**, p 833–846
13. J. Hu and H.L. Tsai, Heat and Mass Transfer in Gas Metal Arc Welding. Part II: The Metal, *Int. J. Heat Mass Transf.*, 2007, **50**, p 808–820
14. S.J. Unfried, C.M. Garzón, and J.E. Giraldo, Numerical and Experimental Analysis of Microstructure Evolution During Arc Welding in Armor Plate Steels, *J. Mater. Process. Technol.*, 2009, **209**, p 1688–1700
15. H.K.D.H. Bhadeshia, Thermal History Analysis of Friction Stir Processed and Submerged Friction Stir Processed Aluminum, *Met. Sci.*, 1982, **16**, p 159–166
16. K.C. Russell, Linked Flux Analysis of Nucleation in Condensed Phases, *Acta Metall.*, 1968, **16**, p 761–769
17. K.C. Russell, Grain Boundary Nucleation Kinetics, *Acta Metall.*, 1969, **17**, p 1123–1131
18. M. Takahashi and H.K.D.H. Bhadeshia, A Model for the Microstructure of Some Advanced Bainitic Steels, *Mater. Trans.*, 1991, **32**, p 689–696
19. G.J. Davies and J.G. Garland, Solidification Structures and Properties of Fusion Welds, *Int. Metall. Rev.*, 1975, **20**, p 83–108
20. H.K.D.H. Bhadeshia, L.-E. Svensson, and B. Gretoft, A Model for the Development of Microstructure in Low-Alloy Steel (Fe-Mn-Si-C) Weld Deposits, *Acta Metall.*, 1985, **33**, p 1271–1283
21. S.J. Jones and H.K.D.H. Bhadeshia, Kinetics of the simultaneous decomposition of austenite into several transformation products, *Acta Mater.*, 1997, **45**, p 2911–2920
22. P. Kruger, On the Relation Between Non-isothermal and Isothermal Kolmogorov-Johnson-Mehl-Avrami Crystallization Kinetics, *J. Phys. Chem. Solids*, 1993, **54**, p 1549–1555
23. M. Grujicic, B. Pandurangan, C.-F. Yen, and B.A. Cheeseman, Modifications in the AA5083 Johnson-Cook Material Model for Use in Friction Stir Welding Computational Analyses. *J. Mater. Eng. Perform*. 2011. doi:10.1007/s11665-011-0118-7
24. M. Grujicic, G. Arakere, B. Pandurangan, J.M. Ochterbeck, C-.F. Yen, B.A. Cheeseman, A.P. Reynolds, and M.A. Sutton, Computational Analysis of Material Flow During Friction Stir Welding of AA5059 Aluminum Alloys, *J. Mater. Eng. Perform*. 2011, doi:10.1007/s11665-011-0069-z
25. M. Grujicic, G. Arakere, A. Hariharan, B. Pandurangan, C-F.Yen and B. A. Cheeseman, "*Two-level Weld-Material Homogenization Approach for Efficient Computational Analysis of Welded Structure Blast Survivability*," Journal of Materials Engineering and Performance, DOI: 10.1007/s11665-011-9876-5, 2010
26. M. Grujicic, G. Arakere, A. Hariharan, and B. Pandurangan, A Concurrent Product-Development Approach for Friction-Stir Welded Vehicle-Underbody Structures, *J. Mater. Eng. Perform.*, 2012, **21**, p 437–449
27. M. Grujicic, G. Arakere, B. Pandurangan, A. Hariharan, C.-F. Yen, B.A. Cheeseman, and C. Fountzoulas, Computational Analysis and Experimental Validation of the Ti-6Al-4V Friction Stir Welding Behavior, *J. Eng. Manuf.*, 2010, **224**, p 1–16
28. M. Grujicic, G. Arakere, B. Pandurangan, A. Hariharan, C.-F. Yen, and B.A. Cheeseman, Development of a Robust and Cost-effective Friction Stir Welding Process for Use in Advanced Military Vehicle Structures, *J. Mater. Eng. Perform.*, 2011, **20**, p 11–23
29. M. Grujicic, G. Arakere, C.-F. Yen, and B.A. Cheeseman, Computational Investigation of Hardness Evolution during Friction-Stir Welding of AA5083 and AA2139 Aluminum Alloys, *J. Mater. Eng. Perform.*, 2011, **20**, p 1097–1108
30. M. Grujicic, G. Arakere, H.V. Yalavarthy, T. He, C.-F. Yen, and B.A. Cheeseman, Modeling of AA5083 Material-Microstructure Evolution During Butt Friction-stir Welding, *J. Mater. Eng. Perform.*, 2010, **19**, p 672–684
31. M. Grujicic, T. He, G. Arakere, H.V. Yalavarthy, C.-F. Yen, and B.A. Cheeseman, Fully-Coupled Thermo-mechanical Finite-element Investigation of Material Evolution During Friction-Stir Welding of AA5083, *J. Eng. Manuf.*, 2010, **224**, p 609–625
32. G.R. Johnson and W.H. Cook, A Constitutive Model and Data for Metals Subjected to Large Strains, High Strain Rates and High Temperatures, *Proceedings of the 7th International Symposium on Ballistics*, 1983
33. ABAQUS Version 6.10EF, User Documentation, Dassault Systems, 2011
34. MATLAB, *The Language of Technical Computing*, 7th ed., The MathWorks Inc, Natick, MA, 2006
35. M. Gore, M. Grujicic, and G.B. Olson, Thermally Activated Grain Boundary Motion Through a Dispersion of Particles, *Acta Metall.*, 1989, **37**, p 2849–2854
36. J.W. Elmer, J. Wong, and T. Ressler, Spatially Resolved X-ray Diffraction Mapping of Phase Transformations in the Heat-Affected Zone of Carbon-Manganese Steel Arc Welds, *Metall. Mater. Trans. A*, 2001, **32**, p 1175–1187
37. M. Grujicic, B. Pandurangan, K.L. Koudela, and B.A. Cheeseman, A Computational Analysis of the Ballistic Performance of Light-Weight Hybrid-Composite Armors, *Appl. Surf. Sci.*, 2006, **253**, p 730–745
38. M. Grujicic and W.S. Owen, Models for Short Range Order in an f.c.c. Fe-Ni-Cr Alloy with a High Concentration of Nitrogen, *Acta Metall. Mater.*, 1995, **43**, p 4201–4211